Available online at www.sciencedirect.com
SCIENCE DIRECT
International Journal of Mass Spectrometry 252 (2006) 38–46
International Journal of Mass Spectrometry
www.elsevier.com/locate/ijms

Mass spectrometric and modeling investigations of bimetallic silver–cobalt clusters

Ewald Janssens [a], Thibaut Van Hoof [b], Nele Veldeman [a], Sven Neukermans [a], Marc Hou [b], Peter Lievens [a,*]

[a] *Laboratorium voor Vaste-Stoffysica en Magnetisme, K.U. Leuven, Celestijnenlaan 200 D, B-3001 Leuven, Belgium*
[b] *Physique des Solides Irradiés et des Nanostructures, CP 234, Université Libre de Bruxelles, Campus de la Plaine, Boulevard du Triomphe, B-1050 Brussels, Belgium*

Received 25 November 2005; received in revised form 31 December 2005; accepted 2 January 2006
Available online 28 February 2006

Abstract

The stability of bimetallic silver–cobalt clusters with less than 50 atoms is studied experimentally and their associated geometries are predicted by classical modeling. The clusters are created by laser vaporization and inert gas condensation. Their mass distribution is analyzed with time-of-flight mass spectrometry. For clusters containing mainly silver, we find strong quantum size effects related to itinerant behavior of the silver and cobalt valence electrons. In the case of clusters containing mainly cobalt, no pronounced size effects appear in the mass spectra. Photofragmentation experiments reveal that neutral silver atom evaporation is the favorable channel, suggesting that the Ag─Co bonds are weaker than the Co─Co bonds. Consistently, and for both sets of clusters, Metropolis Monte-Carlo simulations predict these clusters to have icosahedral based structures that may depend on temperature. In clusters containing mainly silver, cobalt sits at the cluster center and fragmentation proceeds by the evaporation of silver surface atoms. In clusters containing mainly cobalt, silver atoms also locate at the periphery and are more weakly bound to the cluster than cobalt surface atoms.

Keywords: Metal cluster; Fragmentation; Molecular dynamic; Bimetallic

1. Introduction

Bimetallic clusters are exciting research objects, since they can have structures and phases different from both pure metal clusters and bulk alloy configurations. In addition they allow for the investigation of mixtures of metals that are non-miscible in the bulk. By tuning not only the size but also the stoichiometry of the clusters, a rich variety of structures and phases can be investigated. In particular clusters composed of open d shell transition metal atoms and coinage metal atoms are appealing. They possibly can be used in applications such as catalysis and optics [1–3] and can have remarkable segregated structures such as core-shell symmetries [3–6] or layered structures [8]. The component with the lowest surface energy is expected to accumulate preferentially at the surface to minimize the total energy. A transition metal dopant with a small atomic radius located in the center of an icosahedral coinage metal cluster can relax the strain and enhance the melting temperature [7].

Silver and cobalt are completely immiscible in the bulk. Also in nanometer sized Ag_nCo_m clusters segregation is expected for thermodynamic reasons. The surface energy of silver is almost a factor of two smaller than that of cobalt, and the silver atomic radius (1.44 Å) is noticeable larger than the cobalt atomic radius (1.25 Å). Bimetallic clusters are expected to have a majority of silver atoms at the surface. The existence of a core-shell structure has been investigated for gas phase Ag_nCo_m clusters. Segregation was found, although the protection of the cobalt core by the silver surface layer was not complete for 3 nm diameter particles [9]. The optical properties of mixed Ag_xCo_{1-x} particles embedded in an alumina matrix confirmed the existence of a core-shell structure [3]. The preference for silver to be positioned at low coordinated sites is also found in Metropolis Monte-Carlo simulations on Ag_nCo_{201-n} clusters with different stoichiometries [10].

* Corresponding author. Tel.: +32 16 327207; fax: +32 16 327983.
E-mail addresses: mhou@ulb.ac.be (M. Hou), peter.lievens@fys.kuleuven.be (P. Lievens).

1387-3806/$ – see front matter © 2006 Elsevier B.V. All rights reserved.
doi:10.1016/j.ijms.2006.01.009

The electronic and magnetic properties of binary transition metal–coinage metal clusters are very complex due to the presence of the unfilled d shells [11,12]. The magnetic and electronic properties of metallic nanoparticles have a quantum mechanical origin. Therefore, detailed ab initio calculations are needed for an accurate description [4,13–16]. On the other hand the structure, morphology, segregation, and phase transitions of nanoparticles have been successfully modeled with classical mechanics and thermodynamics. Direct comparison with experiments showed that classical modeling successfully predicts the structure of unsupported clusters or nanoclusters in a matrix [5,6,10,17–19] and their kinetic and dynamical properties on a substrate [19–21]. However, since the structure is determined by quantum mechanics through the underlying electronic structure, classical modeling must have its limitations.

It the present paper we combine experimental measurements with classical modeling to study the stability and morphology of pure Ag_n, Co_m, and bimetallic Ag_nCo_m clusters with less than 50 atoms. The cluster production technique and analysis methods are summarized in Section 2. The structure of clusters with selected sizes is calculated classically with Metropolis Monte-Carlo (MMC) simulations. The computational method is described in Section 3. The next three sections present the experimental and modeling results and the discussions. First, pure Ag_n and Co_m clusters are dealt with (Section 4), then bimetallic Ag_nCo_m clusters containing mainly silver ($n \gg m$, Section 5) and mainly cobalt ($m \gg n$, Section 6). The conclusions are formulated in Section 7.

2. Experimental method

The bimetallic clusters are produced in a home-built dual-target dual-laser vaporization source. Heterogeneous clusters with a wide variety in size and composition can be produced in this source [22–24], which is described in detail elsewhere [25]. Silver and cobalt rectangular plate targets are moved in a closed-loop pattern during cluster production. The material is ablated by the focussed second harmonic output of a pulsed Nd:YAG laser. A different laser is used for each target to allow independent adjustment of laser powers and evaporation times. The evaporated cloud of atoms is entrained in a short pulse of cold helium gas. Cluster formation is initiated by collisions between vaporized atoms and the inert gas inside a small formation chamber. Subsequently, the mixture of atoms, clusters and inert gas undergoes a supersonic expansion into vacuum. The expansion reduces the temperature of the clusters and because of the rapidly decreasing density the cluster growth stops.

For the mixed clusters, we deal with clusters composed of a main material incorporating one or a few dopant atoms. The stoichiometry of the clusters formed is controlled by the time delay between the vaporization lasers and the laser power density.

Four types of clusters are investigated: homogeneous Ag_n and Co_m clusters and heterogeneous Ag_nCo_m systems with $n \gg m$ and with $m \gg n$. An extension of the formation chamber was needed for the creation of homogeneous Ag_n and heterogeneous Ag_nCo_m with $n \gg m$ systems. The enlarged formation chamber allows for more collisions and reflects the weak cluster formation probability of silver atoms that might be related to the low binding energy of silver clusters.

The positively charged clusters are accelerated, mass separated in the field free drift region of a reflectron time-of-flight mass spectrometer, and recorded by a microchannel plate detector. A pulsed electrostatic deflector for mass selection is located in the field free region before the reflectron. This mass selector is similar to the one developed by Vlasak and coworkers [26]. When a package of interest arrives at the deflector, the field is pulsed off to allow the selected package to be transmitted.

Neutral clusters are postionized with an excimer laser. The laser fluence is a critical parameter. In the low fluence regime (less than 0.5 mJpp/cm^2), the presence of multiphoton processes is unlikely and single photon ionization will be the main channel to create cationic species. In the high fluence regime (more than 5 mJpp/cm^2), the clusters are heated by multiphoton absorption. This heat is released by rapid sequential evaporations of hot atoms and electrons in the extraction region. After these evaporation processes more stable clusters will be more abundant. During the subsequent drift period, metastable parent cluster ions can undergo further evaporation (*delayed fragmentation*) with parent and fragment particles proceeding at the center of mass velocity [27]. In the retarding field of the reflectron they are spatially separated, the fragment ions turn faster than the parent molecules. In combination with the mass selector the delayed fragmentation of selected parent molecules can be investigated.

Two different nanosecond excimer lasers are used for photoionization and photofragmentation: an F_2 excimer laser (7.9 eV photons, maximum pulse energy 1.6 mJ) and an ArF excimer laser (6.4 eV photons, maximum pulse energy 150 mJ), both operated at a 10 Hz repetition rate.

3. Computational method

Metropolis Monte-Carlo importance sampling with a semi-empirical potential is used to predict the thermodynamic equilibrium configuration of Ag_nCo_m clusters with a given composition. The atomic configuration of each cluster is checked at two different temperatures, 50 and 300 K. As will be shown, this allows to detect possible isomers. The MMC configurations are quenched by molecular statics (MS) toward a nearby local minimum. The MS calculations employ the same potential as MMC for evaluating the forces on each atom. The atoms move freely if the scalar product between force and velocity is positive. Otherwise, their velocity is set to zero. This method was already used in order to predict the configurations of mixed Ag_nCo_m ($200 < n + m < 3000$) clusters with different stoichiometries [10,28]. The quantum mechanical nature of the electronic structure is not accounted for in the calculations; the MMC sampling as well as the MS trajectories are purely classical. This approach is supposed to better reproduce the properties of large systems than of small ones, for which configurations may be dominated by quantum size effects. The main advantages of the classical modeling are the speed of calculation, being orders of magnitude faster than the speed of ab initio methods, and the possibility to investigate the role of temperature on the equilibrium geometry.

The semi-empirical classical potential contains two terms. The first describes the repulsive pair interaction between the atomic cores and the second is the attractive N-body interaction resulting from the valence electron clouds. The embedded atom model (EAM) potential [29] parameterized on the basis of the equation of states of Rose et al. [30] according to Ref. [31] is used in the present work. It was assessed on the properties of Ag–Co mixed systems as discussed in Ref. [21]. This potential does not account for excess charge. The limitations and validity of the EAM potential are discussed below by means of comparisons with results in literature.

The MMC sampling is achieved in the canonical ensemble (fixed composition, pressure, and temperature). The sampling scheme includes two types of trials: (i) random displacement of each atom in the cluster from its actual position and (ii) random site exchange between two chemically different atoms. A trial is accepted if it lowers the configuration energy of the system. If the configuration energy is increased, trials are accepted with a probability proportional to a Boltzman factor: $P = e^{-\Delta U/kT}$ where ΔU is the configuration energy difference. The magnitude of the displacements in (i) is dynamically adjusted in order to maintain a rate of acceptance close to 0.4, which is empirically found to optimize convergence. Trials of type (ii) correspond to non-physical evolution paths but they limit the risk of trapping the system into a local minimum separated from a lower lying minimum by a high energy barrier.

4. Pure cobalt and silver clusters

The properties of homogeneous silver and cobalt clusters differ strongly. The main reason for this difference is the occupancy of the valence d shell, which is completely filled for silver ($4d^{10}5s^1$), and has three ($3d^74s^2$) or two ($3d^84s^1$) vacancies in a cobalt atom. Silver is often considered a simple metal in the sense that its chemistry is dominated by the single 5s valence electron, while the filled 4d shell represents only a small perturbation. In cobalt clusters the partially filled d shell is of major importance for the electronic and magnetic structure [32,33].

4.1. Mass spectrometric results

Mass spectra of positively charged silver and cobalt clusters after fragmentation using high fluence laser light (6.4 eV photons, fluence 20.0 mJpp/cm^2) are shown in Fig. 1. The mass distribution of the resulting fragments uncovers stability information since the formation of more stable clusters is more likely after fragmentation [22].

The peak maxima for Ag_n^+ are strongly size dependent (solid line in Fig. 1a). The intensity variations reveal an odd–even staggering (the abundance is higher if n is odd) and steps after Ag_n^+ with $n = 3, 9, 21, 41$, and 59. These observations can qualitatively be interpreted within an electronic shell model. In a cluster the single valence s electron of each silver atom is loosely bound and delocalizes over the entire volume. Since cations have one conduction electron less than neutral clusters, the major features in the mass spectra are associated with the closing of electronic shells at total electron numbers 2, 8, 20, 40, and 58. This shell

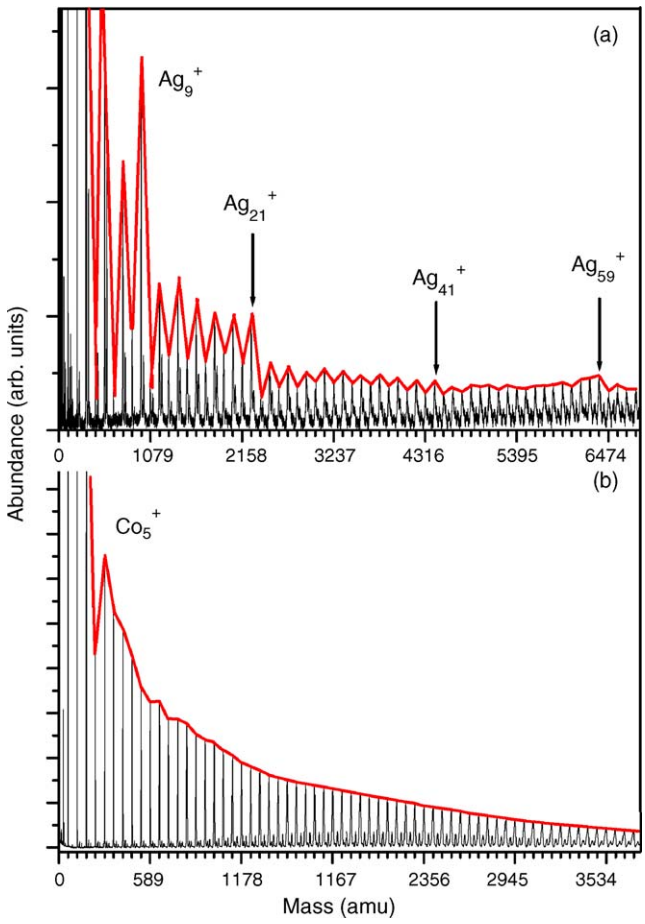

Fig. 1. Mass spectra of (a) Ag_n^+ and (b) Co_m^+ clusters after high fluence photofragmentation (6.4 eV photons). The peak maxima are connected by a solid line. Steps in abundance occur after the named sizes.

structure has been observed before [24,34–36] and explained by different shell models [37], among which the famous jellium model [38]. The smaller peaks following the silver cations in Fig. 1a are delayed fragments of the silver clusters with one atom more. The delayed fragmentation of mass selected mixed clusters is discussed in detail in Sections 5.1 and 6.1. For larger sizes there is a small amount of doubly charged clusters present, Ag_m^{2+} with $m > 80$ (in the mass spectrum in between Ag_m^+ with $m > 40$). There are very few oxygen contaminated clusters present in the silver mass spectrum. The photofragmentation spectrum of Co_m^+ clusters (Fig. 1b) does not show strong size effects, except for an enhanced intensity of Co_5^+. Because of the high density of states at the Fermi level, Co_m^+ clusters do not display a pronounced electronic shell structure [32]. Their size-dependent stability is mainly governed by geometrical factors. The smaller signals in between the pure cobalt clusters correspond to Co_mO^+ and doubly charged Co_m^{2+} species. The oxygen atoms originate from the oxidized target surface and from impurities in the helium carrier gas.

4.2. Structure modeling

Small cobalt clusters have been studied computationally by several groups [33,39,40]. Most of the calculations consider

clusters of a given geometric structure where interatomic distances are either those of the bulk or those obtained after a uniform local relaxation process starting from the bulk lattice constant. Ab initio calculations were performed for very small systems only ($n<8$) [39], because of the difficulty in properly treating the d electrons what results in a slow convergence of the self consistent procedure. In addition, it is hard to find unique ground state structures because of the existence of many almost isoenergetic isomers.

It was shown that small cobalt clusters are compact with a maximal amount of directional bonds between the rather localized d orbitals of neighboring atoms [39]. Rodríguez-López et al. employ a symbiotic algorithm including the semi-empirical interatomic potential of Gupta to predict an icosahedral based growth pattern, reaching the main and intermediate icosahedral sizes at 7, 13, 19, 23, 26, 34, 43, and 55 atoms [33]. This outcome is confirmed by photoelectron spectroscopy on anionic Co_m^- clusters that suggest an icosahedral growth pattern, except for some octahedral sizes (Co_{16}^- to Co_{19}^-) [32]. On the other hand reactivity studies in which clusters are titrated with molecular nitrogen predict close-packed structures for Co_m ($m=3$–16) [40]. It is, however, not completely clear how much the absorption of nitrogen causes the clusters to change their structure.

We investigated the equilibrium configurations of Co_m ($m=4$–10, 13) with classical modeling. Resulting geometries are presented in Fig. 2 together with their symmetry groups and average bond lengths. They are compared with the results obtained by Rodríguez-López et al. [33]. Identical configurations are found with both methods and the average bond lengths are almost the same. Thus, the results obtained using different potentials are consistent with each other.

An icosahedron can be seen as a structure composed of two decahedrons with a $\pi/5$ relative rotation of the pentagonal planes and a common vertex in the center. The geometry of Co_7 is a decahedron. This decahedral structure is also present in Co_9 (see thick lines of Co_9 in Fig. 2) but the five-fold symmetry is broken by the two additional atoms. The latter are located on contiguous facets situated at the same side of the pentagonal plane, that way beginning the formation of the second pentagonal atomic layer of an icosahedron. The tenth atom and the next ones contribute to complete the second pentagonal layer, to reach a perfect icosahedron for Co_{13}. The Co–Co bond length in Co_{13} (2.44 Å) is in good agreement with the DFT result (2.49 Å) in Ref. [12].

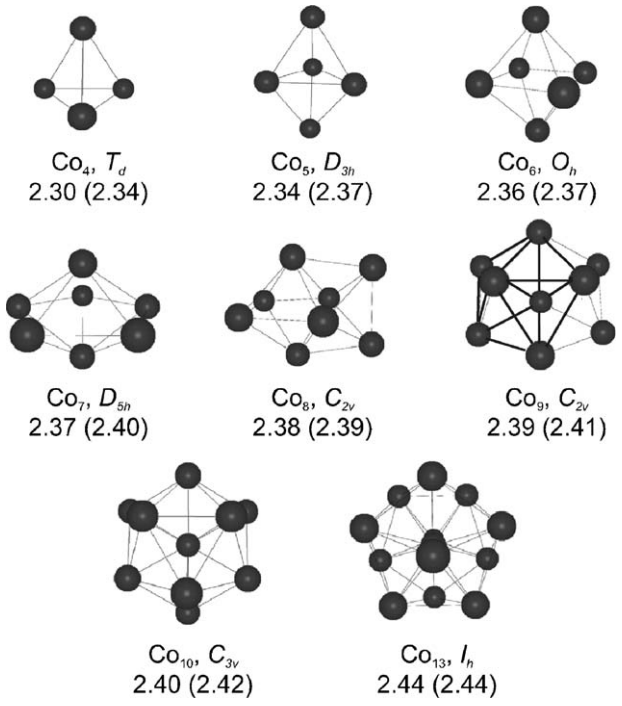

Fig. 2. Geometries of Co_m ($m=4$–10, and $m=13$) obtained with the MMC method. Symmetry groups and averaged Co–Co bond distances (in Å) are given. The numbers between brackets are the bond distances found in Ref. [33].

Also the geometry of small Ag_n ($n=4$–10, 13) clusters was examined with classical modeling. The symmetry and the average bond lengths are summarized in Table 1. The same symmetries are obtained for Ag_n and Co_n for all investigated sizes. The only difference concerns the average Ag–Ag bond length that is about 10% longer than the average Co–Co bond length. The configurations of Ag_n obtained in this work are in perfect agreement with other molecular dynamics simulations by Erkoç and Yilmaz [42]. Their results are obtained with pair potential energy functions, which are however less accurate in predicting the properties of small metallic systems. Here again, the results are found to be insensitive to the applied potential.

Table 1
Symmetry group and averaged Ag–Ag bond length, $\bar{r}$, of neutral Ag_n ($n=4$–10, 13) clusters obtained by classical modeling in this work

n	Classical		Ab initio [41]		Higher energy isomer [41]		
	Symmetry	$\bar{r}$ (Å)	Symmetry	$\bar{r}$ (Å)	Symmetry	$\bar{r}$ (Å)	ΔE (eV)
4	T_d	2.58	D_{2h}	2.69, 2.72	D_{2d}	2.75, 2.81	0.29, 0.33
5	D_{3h}	2.63	D_{2d}	2.65, 2.69	D_{3h}	2.73, 2.78	0.25, 0.54
6	O_h	2.65	C_{2v}	2.79, 2.80			
7	D_{5h}	2.67	D_{5h}	2.74, 2.81			
8	C_{2v}	2.68	C_s	2.74, 2.81	C_{2v}	2.89, 2.86	0.14, 0.06
9	C_{2v}	2.69	D_{3h}	2.99, 2.80	C_{2v}	2.74, 2.81	0.11, 0.05
10	C_{3v}	2.70	C_{3v}	2.76, 2.85			
13	I_h	2.77					

The fourth and fifth column give the symmetry groups and bond lengths (MP2-level, DFT-level, respectively) of cationic Ag_n^+ clusters found in Ref. [41]. If the isomers found in this work and in Ref. [41] differ, a stable isomer close to the classical modeling result is given in the sixth and seventh column together with the energy difference, ΔE, compared to the ground state in Ref. [41].

The structures of the neutral silver clusters are compared in Table 1 with the structures of cationic Ag_n^+ ($n<12$) clusters predicted by Weis et al. [41] with ion mobility measurements in combination with ab initio calculations (both with MP2 and density functional theory (DFT)). For some sizes the classical configurations agree with the ab initio results ($n=7$, 10), while for other sizes ($n=8$, 9) the classical results correspond to isomers that are ab initio predicted to be stable but not obtained as ground state. The most important difference between both methods is found for the smallest clusters ($n=4$–6). In this size range the ab initio calculations predict an energetic competition between 2D and 3D structures, while classical modeling gives 3D close-packed geometries. It is important to note that the positive charge, which cannot be included in the MMC simulations, can have an important influence on the geometry. The fair agreement between the neutral and the cationic clusters in Table 1 suggests that in the present case the charge state is not decisive for the geometry, except possibly for the smallest clusters.

5. Clusters containing mainly silver

5.1. Mass spectrometric results

The mass spectra of Ag_nCo^+ ($n=3$–31) clusters are presented in Fig. 3. The grid lines designate the pure Ag_n^+ clusters. The peaks corresponding to Ag_nCo^+ are connected by a solid line. The isotopomeric distribution of silver (51.8% ^{107}Ag, 48.2% ^{109}Ag) strongly broadens the mass peaks, especially for larger clusters. The combination of the small mass difference between Ag and Co_2, the broad mass peaks, and the limited signal for $Ag_nCo_2^+$ makes it difficult to distinguish $Ag_{n-1}Co_2^+$ from Ag_n^+. Therefore, multiple cobalt doped species are not considered.

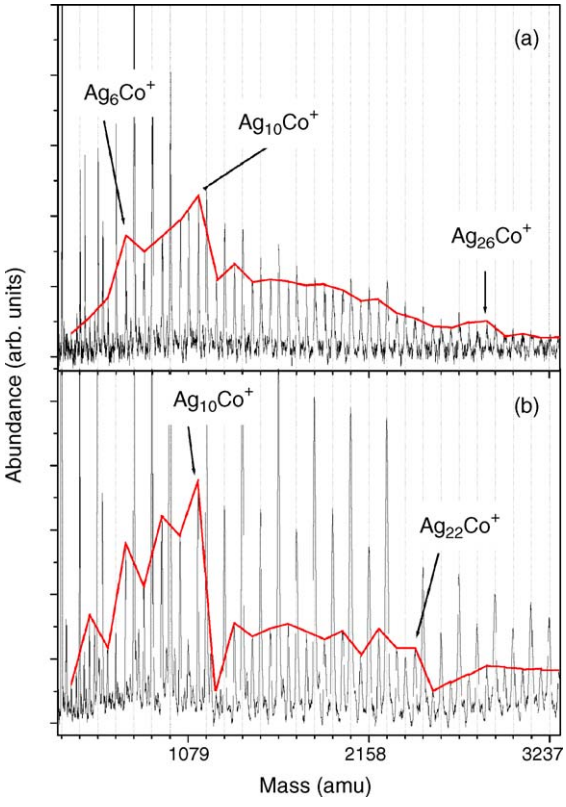

Fig. 3. Mass spectra of mixed $Ag_nCo_m^+$ ($n \gg m$), (a) photoionized using 7.9 eV photons at low laser fluence (0.5 mJpp/cm^2) and (b) photofragmented using 6.4 eV photons at high laser fluence (15 mJpp/cm^2). Grid lines mark the Ag_n^+ ($n=2$–32) clusters. The peaks in between the pure clusters correspond to Ag_nCo^+ and are connected by a solid line.

Fig. 3a shows that all Ag_n and Ag_nCo sizes could be ionized using 7.9 eV photons at low laser fluence (0.5 mJpp/cm^2). On the other hand the ionization efficiency of 6.4 eV photons is small (not on figure). Size-dependent intensity variations in Fig. 3a are present but weak. Local maxima for Ag_6Co, $Ag_{10}Co$, and $Ag_{26}Co$ can either be attributed to a higher yield of these cluster sizes or to a higher ionization efficiency. The most pronounced size-dependent feature, a maximum followed by a strong drop of photoion signal, occurs for $Ag_{10}Co$. Strong abundance fluctuations related to size-dependent stability are unlikely to show up if clusters are produced with a laser vaporization cluster source (although not impossible as shown in Ref. [23]). Therefore, one could favor the explanation of this feature as corresponding to a lower ionization energy of the neutral $Ag_{10}Co$, which is according to expectations if this cluster is considered as an 18 + 1 electron open shell cluster (see below).

The mass distribution of photofragmented Ag_nCo^+ clusters using high fluence 6.4 eV laser light is given in Fig. 3b. The Ag_nCo^+ pattern is non-monotonic and shows a clear odd–even staggering, with maxima for n even. This behavior is caused by an electronic shell structure present in the clusters and is related to the itinerant behavior of the cobalt and silver valence electrons as was discussed in Ref. [16]. The most pronounced feature in the mass spectra, the maximum at $Ag_{10}Co^+$, is due to a remarkable stability. According to DFT calculations, this cluster consists of a Ag_{10}^+ cage with cobalt at the cage center. The positively charged cobalt atom binds to all 10 silver atoms to fulfill the 18-electron rule for transition metals. The nine highest occupied molecular orbitals of $Ag_{10}Co^+$ resemble the 1s, 1p, and 1d spherical levels in the shell model, therefore all nine cobalt valence electrons ($3d^74s^2$) can be considered as itinerant to attain closed electronic shells (total of 18 delocalized electrons). The closed electronic shell structure corresponds to the quenching of the magnetic moment [16].

The intensity ratio of $Ag_{n-1}Co^+$ to Ag_n^+ is larger for low fluence ionization using 7.9 eV photons (Fig. 3a) than for high fluence photofragmentation using 6.4 eV photons (Fig. 3b). For the doped clusters the ionization efficiency with 7.9 eV photons is probably higher than for the pure silver clusters (none of the clusters can be ionized using a single 6.4 eV photon), since the ionization energy of cobalt clusters is lower than the one of silver clusters [34,43]. However, ionization energies are expected to be strongly size dependent and measurements are needed to clarify the issue completely. The $Ag_{n-1}Co^+$ to Ag_n^+ ratio could be slightly enhanced by further increasing the 6.4 eV laser fluence indicating that evaporation of cobalt atoms by heating the clusters is not preferred. We examine this further below.

Some Ag_nCo^+ clusters were mass selected and their delayed fragmentation after intense (20 mJpp/cm^2) 6.4 eV laser irradia-

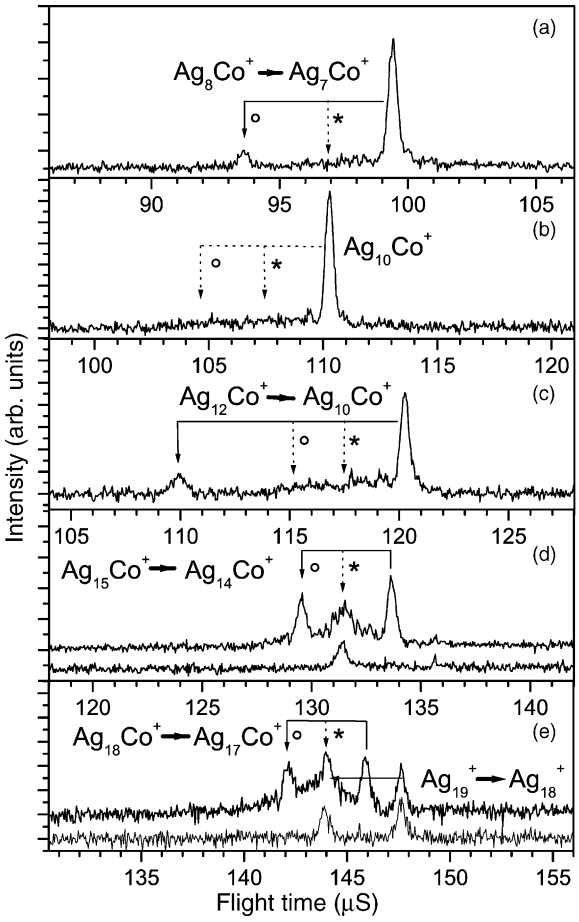

Fig. 4. Delayed fragmentation of Ag_8Co^+ (a), $Ag_{10}Co^+$ (b), $Ag_{12}Co^+$ (c), $Ag_{15}Co^+$ (d), and $Ag_{18}Co^+$ (e). The main fragmentation channel is given by a solid arrow and labeled. The expected position of the mass peaks after loss of silver and cobalt monomers are marked with (◯) and (*), respectively. The bottom curves in panels (d) and (e) are signals recorded without cobalt in the cluster beam and give fragmentation paths of the pure Ag_{n+1}^+ clusters.

tion was recorded as shown in Fig. 4. As for pure silver clusters [44], the preferred fragmentation channel appears to be size dependent. Ag_8Co^+ decays mainly by neutral silver dissociation. $Ag_{10}Co^+$ does not show any delayed fragmentation, which is consistent with the special stability of this cluster [16]. For $Ag_{12}Co^+$ the main dissociation channel is the evaporation of a silver dimer, to reach the stable $Ag_{10}Co^+$. The successive evaporation of two silver monomers is not very likely, since in that case also a significant amount of $Ag_{11}Co^+$ fragments should be recorded. Neutral dimer evaporation has been observed before in dissociation studies of monometallic sodium, silver, and gold cationic clusters [27,44,45]. For the larger clusters, cf. Ag_nCo^+ with $n = 15$ and 18, a perfect mass selection was not possible, some Ag_{n+1}^+ clusters also pass the mass selector. As a reference, the fragmentation signal without any cobalt in the cluster beam was recorded (bottom curves in Fig. 4d and e). The main fragmentation channel for $Ag_{15}Co^+$ and $Ag_{18}Co^+$ is the evaporation of a neutral silver atom. However, due to imperfect mass selection, the loss of a cobalt atom cannot be excluded for these sizes. A Ag_n^+ fragment of Ag_nCo^+ has almost the same time-of-flight as a Ag_n^+ fragment of Ag_{n+1}^+.

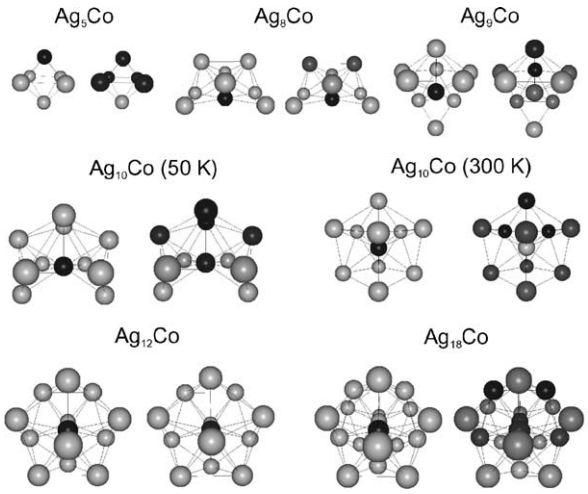

Fig. 5. Atomic configurations of selected Ag_nCo clusters as predicted by classical modeling. On the left side, atoms are shaded as function of their chemical nature: dark for cobalt and light for silver. On the right side, atoms are shaded as a function of the energy needed to remove them from the cluster, the darker the higher the binding energy.

Ag_nCo^+ clusters preferentially decay by losing silver, the cobalt dopant is strongly bound. Quantum size effects are important and determine whether monomer or dimer fragments (or no fragmentation at all) are most likely.

5.2. Modeling and discussion

The most likely fragmentation channel depends on the atomic arrangement of the cluster. All investigated sizes are predicted by classical MMC to have 3D close-packed structures at 50 K and at 300 K, as shown in Fig. 5. Only for $Ag_{10}Co$ the 50 and 300 K configurations are different.

Ag_5Co has a 3D geometry with C_{4v} symmetry. However, this symmetry was not stable in DFT calculations, which predict almost isoenergetic 2D and semi-planar isomers [46]. Probably details of the electronic structure and finite size effects that cannot be included in the classical modeling, determine the geometry of this small cluster.

For $Ag_{10}Co$ the MMC at 50 K gives an open Ag_{10} structure with cobalt at the center. The configuration calculated at a temperature of 300 K consists of a closed Ag_{10} cage around a central cobalt atom. The 0 K energy difference between these two configurations is only 0.02 eV, implying that both structures may be coexisting isomers. The structure obtained at 300 K agrees with the endohedral bicapped tetragonal antiprism, which was found earlier in DFT calculations on the cationic $Ag_{10}Co^+$ cluster [16]. Although smaller Ag–Co bond distances are obtained classically (between 2.46 and 2.55 Å) than with DFT (between 2.62 and 2.73 Å). For other Ag_nCo ($n \neq 5, 10$) no ab initio results are available.

The structure of Ag_8Co (C_{2v}) is close to the one of Ag_9, while Ag_9Co (C_s) is different from Ag_{10}. In both clusters the dopant locates at the highest coordinated site of an incomplete silver cage. $Ag_{12}Co$ is an icosahedron with the cobalt atom surrounded by 12 silver atoms and a 2.62 Å Ag–Co interatomic distance. The

larger $Ag_{18}Co$ cluster consists of an icosahedron in which the cobalt atom locates at the center plus an umbrella of six atoms. This kind of structures are predicted to have an enhanced stability by the umbrella model [47]; geometrical subshell closures accord with a number of atoms needed for complete coverage of one or more facets of a perfect geometrical shape. A central location of the dopant atom in icosahedral silver clusters has also been obtained recently by Mottet et al. [7]. A small central dopant atom relaxes the strained icosahedral structure and allows to tune the cluster melting temperature.

Fig. 5 also gives the energy maps of the optimized clusters. In an energy map the atoms are shaded according to the atom binding energy, which is the configuration energy difference between the mother and the fragment obtained by removing the atom without relaxation of the structure. A dark shading corresponds to a higher atom binding energy. The energy maps of Ag_5Co, Ag_8Co, $Ag_{12}Co$, and $Ag_{18}Co$ all predict the cobalt atom to be the most strongly bound atom. In Ag_9Co the cobalt atom is not the most strongly bound atom but there are three silver atoms that have a lower binding energy. The energy map of $Ag_{10}Co$ (300 K) and $Ag_{10}Co$ (50 K) are very different. At 300 K the cobalt atom has the lowest binding energy of all atoms, while it has the highest binding energy at 50 K.

A lower cobalt binding energy can be related to a higher stress acting on the dopant. Indeed, the cobalt binding energy decreases along the $Ag_{12}Co$, $Ag_{10}Co$ (50 K), Ag_9Co and $Ag_{10}Co$ (300 K) sequence, consistently with a decreasing averaged Ag–Co bond distance: 2.624, 2.344, 2.300, and 2.293 Å, which corresponds to an increase of stress.

In $Ag_{10}Co$ (300 K) the binding energy of the cobalt atom is weak because of the compression by the silver cage. However, even in this cluster the evaporation of the cobalt atom will not be the most likely fragmentation channel. The energy maps of Fig. 5 give differences in configuration energies though for fragmentation paths also energy barriers are important. Evaporation of silver atoms is more likely because they are at the surface, while the energy barrier for the central cobalt atom to cross the surface is high.

In conclusion, the dissociation of silver atoms is the most likely fragmentation channel for the examined Ag_nCo clusters, which is consistent with the experiments. The classical model, however, cannot predict the observed quantum size effects.

6. Clusters containing mainly cobalt

6.1. Mass spectrometric results

Fig. 6a presents a mass spectrum of cationic $Ag_nCo_m^+$ ($m \gg n$, $n \leq 4$, and $14 \leq m \leq 39$) clusters. The dotted grid lines correspond to pure Co_m^+ clusters. $AgCo_{m-2}^+$ and $Ag_2Co_{m-4}^+$ clusters appear 10 and 20 amu before Co_m^+, respectively.

To concentrate on neutral clusters, charged clusters are electrostatically removed from the beam. By increasing the laser fluence (6.4 eV photons) one can go from the single photon photo-ionization regime towards the multiple photon absorption regime. This fluence dependence is presented in Fig. 6b–d. The curves are scaled vertically inversely proportional to the applied

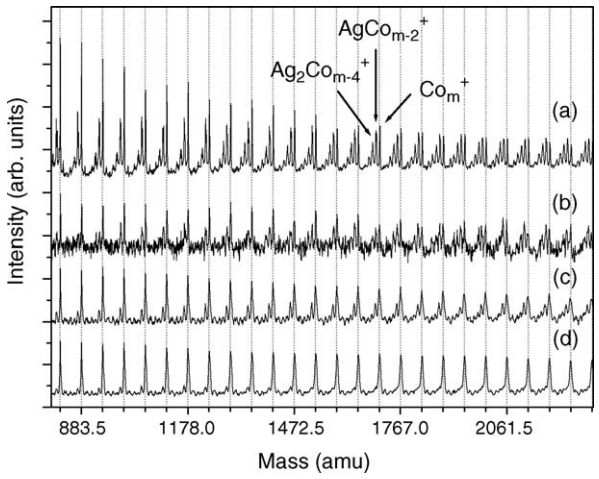

Fig. 6. Mass spectra of mixed Ag_nCo_m ($m \gg n$). The grid lines mark the Co_m^+ ($m = 14$–39) clusters. The peaks in front of the pure Co_m^+ clusters correspond to $AgCo_{m-2}^+$, $Ag_2Co_{m-4}^+$, $Ag_3Co_{m-6}^+$. Spectrum (a) gives the cationic clusters as produced in the source. Spectra (b)–(d) are the postionized neutral clusters as function of an increasing laser fluence: (b) 1 mJpp/cm^2, (c) 3 mJpp/cm^2, and (d) 7 mJpp/cm^2. Spectra (b)–(d) are scaled vertically inversely proportional to the applied laser fluence. Remark the decreasing ratio of $AgCo_{m-2}$ to Co_m clusters with increasing laser fluence.

laser fluence. Two observations can be made: (i) although the signal intensity in the low fluence regime (Fig. 6b) is very small (limited absorption cross-section), most clusters could be ionized. So the ionization energy of those species is lower than the applied 6.4 eV photon energy. Except for the difference in signal intensity, spectrum 6b is similar to the distribution of the cationic clusters (Fig. 6a). Small differences can be attributed to: the larger signal to noise ratio in Fig. 6b, fragmentation processes due to the heating of the clusters by the laser light (see below), or to differences in the initial distribution of the neutral and the cationic clusters. It is generally assumed that the cluster distribution of the neutral and cationic clusters produced in a laser vaporization source are comparable and (ii) the ratio of $AgCo_{m-2}^+$ to Co_m^+ decreases with increasing laser fluence. Most of Ag_nCo_m ($n = 1$, 2, 3) clusters are visible for a fluence of 1 mJpp/cm^2 (Fig. 6b), while their relative intensity decreases dramatically by increasing the laser fluence to 3 mJpp/cm^2 (Fig. 6c) and 7 mJpp/cm^2 (Fig. 6d). The intensity ratio is most likely not dominated by a difference in ionization efficiency since the ionization potential of pure cobalt clusters is lower than 6.4 eV [43]. Most probably the clusters are heated by multiphoton absorption and photofragment. The fragmentation channel having the lowest energy barrier will be preferred. In this case it would mean that silver evaporation is most likely. To strengthen this argumentation, the delayed fragments of some selected sizes are investigated.

Fig. 7 shows the fragmentation channels of the following groups of peaks: Co_m^+, $AgCo_{m-2}^+$, $Ag_2Co_{m-4}^+$ with $m = 15$ (a), 20 (b), 22 (c), and 27 (d). The laser fluence was kept as low as 3 mJpp/cm^2. If higher laser fluences are applied, no $Ag_nCo_m^+$ ($n \geq 1$) species survive; they probably immediately fragment in the extraction region. The four panels of Fig. 7 support the same conclusion. Losing a neutral silver atom is the main fragmenta-

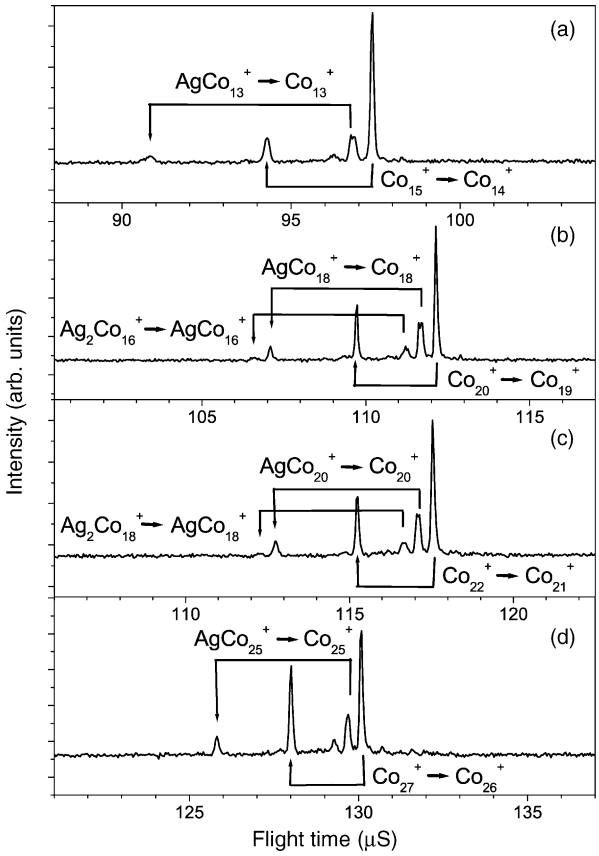

Fig. 7. Delayed fragmentation of mass selected groups of peaks: Co_m^+, $AgCo_{m-2}^+$, and $Ag_2Co_{m-4}^+$ with $m=15$ (a), 20 (b), 22 (c) and 25 (d). All panels show that the main evaporation channel of Co_m^+ is the evaporation of a single cobalt atom, $AgCo_{m-2}^+$ clusters preferentially evaporate the silver dopant.

tion channel for the mixed $Ag_nCo_m^+$ ($m \gg n$), despite the majority of cobalt atoms in the clusters. A limited amount of cobalt evaporation cannot be excluded (cf. tiny signals that appear before the Co_{m-1}^+ fragmentation peaks, which however are clearly not the main fragmentation channel).

One can conclude that the silver atoms are easily removed from $Ag_nCo_m^+$ ($m \gg n$). Most probably the silver atoms locate on the surface of the mixed clusters and heterogeneous Ag–Co bonds are weaker than the homogeneous Co–Co bonds. This is confirmed by modeling in the next section.

6.2. Modeling and discussion

The classical model is applied to investigate the configurations of selected Ag_nCo_m ($m \gg n$) clusters at 50 K and at 300 K. Fig. 8 shows the equilibrium configurations found for Ag_2Co_{13}, Ag_3Co_{12}, $AgCo_{18}$, $AgCo_{20}$, and $AgCo_{25}$. The atomic configuration of Ag_2Co_{13} is an icosahedron of cobalt with the two silver atoms locating at sites on adjacent facets. In Ag_3Co_{12} the additional silver atom replaces a cobalt atom at a vertex of the icosahedron. Only the structure of $AgCo_{18}$ depends on the temperature. At 50 K the 19 atom cluster is an icosahedron with a six-atom umbrella where the silver atom is part of the pentagon in the middle of the cluster. At 300 K the silver atom locates

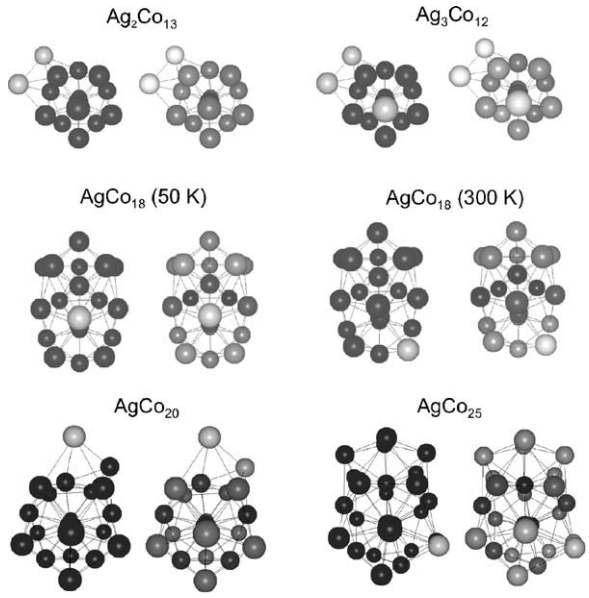

Fig. 8. Atomic configuration of selected Ag_nCo_m ($m \gg n$) clusters as predicted by classical modeling. On the left side, atoms are shaded as function of their chemical nature: dark for cobalt and light for silver. On the right side, atoms are shaded as a function of the energy needed to remove them from the cluster, the darker the higher the binding energy.

in the umbrella. While temperature seems to have an important role on the most probable cluster configuration, the energy difference between the isomers is small (0.16 eV) and in both cases the silver atom locates at the surface. The equilibrium structure of $AgCo_{20}$ is a Co_{19} icosahedron plus umbrella with the additional cobalt and silver atoms on the surface. $AgCo_{25}$ is not symmetric and also has the silver atom at a low coordinated surface position.

The preference for silver atoms to locate at low coordinated positions on the surface is in agreement with the structures obtained for the larger 201-atom clusters (Ag_nCo_{201-n}, $n \ll 201$) [10] and with the formation of core-shell structures in even larger Ag_nCo_m particles [3,9,28]. Similar segregation effects have been found in Co_nCu_m clusters [8,12]. Also there, copper atoms tend to occupy reduced coordination positions on the surface, while cobalt atoms prefer to locate in the interior.

From the energy maps, also shown in Fig. 8, one can see: (i) that low coordinated atoms have, as expected, a smaller binding energy and (ii) that silver atoms are less tightly bound than the cobalt atoms. This result is consistent with the surface energy of bulk silver being much lower than the one of cobalt. It also agrees with the experimental observation that silver atoms evaporate preferentially when heating the clusters with laser light.

7. Conclusion

Mass spectrometric investigations of the stability of mixed $Ag_nCo_m^+$ ($n \gg m$ and $m \gg n$) clusters were performed. It was shown that in both cases the evaporation of neutral silver atoms was the preferred fragmentation channel. For clusters containing mainly silver pronounced finite size effects reveal an electronic shell structure. The configurations of selected cluster sizes were

obtained with classical modeling. The clusters prefer compact 3D arrangements and follow an icosahedral growth pattern. For Ag_nCo_m with $n \gg m$ the cobalt dopants prefer highly coordinated sites and are strongly bound, for clusters with $m \gg n$ the silver atoms are poorly coordinated surface atoms and are loosely bound.

Acknowledgements

This work is supported by the Belgian Interuniversity Poles of Attraction program (IAP/P5/01), the Fund for Scientific Research-Flanders (FWO), and the Flemish Concerted Action (GOA/2004/02). E.J. and S.N. are postdoctoral researchers of the Fund for Scientific Research – Flanders (FWO).

References

[1] U. Kreibig, M. Vollmer, Optical Properties of Metal Clusters, Springer, Berlin, 1995.
[2] K. Koszinowski, D. Schroder, H. Schwarz, Organometallics 23 (2004) 1132.
[3] M. Gaudry, E. Cottancin, M. Pellarin, J. Lermé, L. Arnaud, J.R. Huntzinger, J.L. Vialle, M. Broyer, J.L. Rousset, M. Treilleux, P. Mélinon, Phys. Rev. B 67 (2003) 155409.
[4] G. Rossi, A. Rapallo, C. Mottet, A. Fortunelli, F. Baletto, R. Ferrando, Phys. Rev. Lett. 93 (2004) 105503.
[5] F. Baletto, C. Mottet, R. Ferrando, Eur. Phys. J. D24 (2003) 233.
[6] A. Rapallo, G. Rossi, R. Ferrando, A. Fortunelli, B.C. Curley, L.D. Loyd, G.M. Tarbuck, R.L. Johnston, J. Chem. Phys. 122 (2005) 194308.
[7] C. Mottet, G. Rossi, F. Baletto, R. Ferrando, Phys. Rev. Lett. 95 (2005) 035501.
[8] J. Wang, G. Wang, X. Chen, W. Lu, J. Zhao, Phys. Rev. B 66 (2002) 014419.
[9] L. Favre, S. Stanescu, V. Dupuis, E. Bernstein, T. Epicier, P. Mélinon, A. Perez, Appl. Surf. Sci. 226 (2004) 265.
[10] T. Van Hoof, M. Hou, Eur. Phys. J. D29 (2004) 33.
[11] L.C.C.M. Nagamine, B. Mevel, B. Dieny, B. Rodmacq, J.R. Regnard, C. Revenant-Brizard, I. Manzini, J. Magn. Magn. Mater. 195 (1999) 437.
[12] Q.L. Lu, L.Z. Zhu, L. Ma, G.H. Wang, Chem. Phys. Lett. 407 (2005) 176.
[13] E. Janssens, H. Tanaka, S. Neukermans, R.E. Silverans, P. Lievens, Phys. Rev. B 69 (2004) 085402.
[14] S.Y. Wang, J.Z. Yu, H. Mizuseki, Q. Sun, C.Y. Wang, Y. Kawazoe, Phys. Rev. B 70 (2004) 165413.
[15] M.B. Torres, E.M. Fernández, L.C. Balbás, Phys. Rev. B 71 (2005) 155412.
[16] E. Janssens, S. Neukermans, H.M.T. Nguyen, M.T. Nguyen, P. Lievens, Phys. Rev. Lett. 94 (2005) 113401.
[17] J. Jellinek, E.B. Krissinel, Chem. Phys. Lett. 258 (1996) 283.
[18] E.E. Zhurkin, M. Hou, J. Phys. Condens. Matter 12 (2000) 6735.
[19] B. Pauwels, G. Van Tendeloo, W. Bouwen, L. Theil Kuhn, P. Lievens, H. Lei, M. Hou, Phys. Rev. B 62 (2000) 10383.
[20] P. Jensen, Rev. Mod. Phys. 71 (1999) 1695.
[21] M. Hou, M. El Azzaoui, H. Pattyn, J. Verheyden, G. Koops, G.L. Zhang, Phys. Rev. B 62 (2000) 5117.
[22] S. Neukermans, E. Janssens, H. Tanaka, R.E. Silverans, P. Lievens, Phys. Rev. Lett. 90 (2003) 033401.
[23] S. Neukermans, E. Janssens, Z.F. Chen, R.E. Silverans, P.V.R. Schleyer, P. Lievens, Phys. Rev. Lett. 92 (2004) 163401.
[24] E. Janssens, S. Neukermans, X. Wang, N. Veldeman, R.E. Silverans, P. Lievens, Eur. Phys. J. D34 (2005) 23.
[25] W. Bouwen, P. Thoen, F. Vanhoutte, S. Bouckaert, F. Despa, H. Weidele, R.E. Silverans, P. Lievens, Rev. Sci. Instrum. 71 (2000) 54.
[26] P.R. Vlasak, D.J. Beussman, M.R. Davenport, C.G. Enke, Rev. Sci. Instrum. 67 (1996) 68.
[27] C. Bréchignac, P. Cahuzac, J. Leygnier, J. Weiner, J. Chem. Phys. 90 (1989) 1492.
[28] T. Van Hoof, M. Hou, Phys. Rev. B 72 (2005) 115434.
[29] M.S. Daw, M.I. Baskes, Phys. Rev. B 29 (1984) 6443.
[30] J.H. Rose, J.R. Smith, F. Guinea, J. Ferrante, Phys. Rev. B 29 (1984) 2963.
[31] R.A. Johnson, Phys. Rev. B 41 (1990) 9717.
[32] S.R. Liu, H.J. Zhai, L.S. Wang, Phys. Rev. B 64 (2001) 153402.
[33] J.L. Rodríguez-López, F. Aguilera-Granja, K. Michaelian, A. Vega, Phys. Rev. B 67 (2003) 174413.
[34] G. Alameddin, J. Hunter, D. Cameron, M.M. Kappes, Chem. Phys. Lett. 192 (1992) 122.
[35] I. Katakuse, T. Ichihara, Y. Fujita, T. Matsuo, T. Sakurai, H. Matsuda, Int. J. Mass. Spectrom. Ion Process. 67 (1985) 229.
[36] K.J. Taylor, C.L. Pettiette-Hall, O. Cheshnovsky, R.E. Smalley, J. Chem. Phys. 96 (1992) 3319.
[37] W.A. de Heer, Rev. Mod. Phys. 65 (1993) 611.
[38] W. Ekardt, Phys. Rev. Lett. 52 (1984) 1925.
[39] H.J. Fan, C.W. Liu, M.S. Liao, Chem. Phys. Lett. 273 (1997) 353.
[40] J. Ho, E.K. Parks, L. Zhu, S.J. Riley, Chem. Phys. 201 (1995) 245.
[41] P. Weis, T. Bierweiler, S. Gilb, M.M. Kappes, Chem. Phys. Lett. 355 (2002) 355.
[42] Ş. Erkoç, T. Yilmaz, Physica E 5 (1999) 1.
[43] S. Yang, M.B. Knickelbein, J. Chem. Phys. 93 (1990) 1533.
[44] S. Krückeberg, G. Dietrich, K. Lützenkirchen, L. Schweikhard, C. Walther, J. Ziegler, J. Chem. Phys. 110 (1999) 7216.
[45] M. Vogel, K. Hansen, A. Herlert, L. Schweikhard, Eur. Phys. J. D16 (2001) 73.
[46] E. Janssens, X.J. Hou, M.T. Nguyen, P. Lievens, submitted for publication.
[47] T.P. Martin, Phys. Rep. 273 (1996) 199.